Gas Sensing Properties of CuWO4@WO3 n-n Heterojunction Prepared by Direct Hydrolysis of Mesitylcopper (I) on WO3×2H2O Nanoleaves

Justyna Jońca, Kevin Castello-Lux, Katia Fajerwerg, Myrtil L Kahn, Vincent Collière, Philippe Menini, Izabela Sówka, Pierre Fau

chemosensors

MDPI

Article

Gas Sensing Properties of $CuWO_4$@WO_3 n-n Heterojunction Prepared by Direct Hydrolysis of Mesitylcopper (I) on $WO_3 \cdot 2H_2O$ Nanoleaves

Justyna Jońca [1,*], Kevin Castello-Lux [2], Katia Fajerwerg [2], Myrtil L. Kahn [2], Vincent Collière [2], Philippe Menini [3], Izabela Sówka [1] and Pierre Fau [4,*]

1 Department of Environment Protection Engineering, Faculty of Environmental Engineering, Wrocław University of Science and Technology, 50-377 Wroclaw, Poland
2 Laboratoire de Chimie de Coordination, Centre Nationale de la Recherche Scientifique, CNRS 205 Route de Narbonne, 31400 Toulouse, France
3 Laboratoire d'Analyse et d'Architecture des Systèmes, Centre National de la Recherche Scientifique, Université de Toulouse, UPS, 7 Avenue du Colonel Roche, F-31031 Toulouse, France; menini@laas.fr
4 Laboratoire de Physique et Chimie des Nano-objets, LPCNO-INSA, UMR 5215, 135 Avenue de Rangueil, CEDEX 4, 31077 Toulouse, France
* Correspondence: justyna.jonca@pwr.edu.pl (J.J.); pfau@insa-toulouse.fr (P.F.)

Abstract: The nanometer size Cu_2O@$WO_3 \cdot H_2O$ composite material has been prepared by the direct hydrolysis of mesitylcopper (I) on $WO_3 \cdot 2H_2O$ nanoleaves. The synthesis has been performed in toluene without the addition of any ancillary ligands. The prepared nanocomposite has been deposited as a gas-sensitive layer on miniaturized silicon devices and heated up gradually to 500 °C in the ambient air. During the heating, the $CuWO_4$ phase is formed upon the reaction of Cu_2O with the WO_3 support as revealed by the XRD analyses. The as-prepared $CuWO_4$@WO_3 sensors have been exposed to 10 ppm of CO or 0.4 ppm of NO_2 (RH = 50%). At the operating temperature of 445 °C, a normalized response of 620% towards NO_2 is obtained whereas the response to CO is significantly lower (S = 30%). Under these conditions, the sensors prepared either with pristine CuO or WO_3 nanostructures are sensitive to only one of the two investigated gases, i.e., CO and NO_2, respectively. Interestingly, when the $CuWO_4$@WO_3 sensitive layer is exposed to UV light emitted from a 365 nm Schottky diode, its sensitivity towards CO vanishes whereas the response towards NO_2 remains high. Thus, the application of UV illumination allowed us to modify the selectivity of the device. This new nanocomposite sensor is a versatile sensitive layer that will be integrated into a gas sensor array dedicated to electronic nose platforms.

Keywords: gas sensors; $CuWO_4$@WO_3 nanocomposite; n-n heterojunction; metal–organic synthesis; CO and NO_2 detection; selectivity

Citation: Jońca, J.; Castello-Lux, K.; Fajerwerg, K.; Kahn, M.L.; Collière, V.; Menini, P.; Sówka, I.; Fau, P. Gas Sensing Properties of $CuWO_4$@WO_3 n-n Heterojunction Prepared by Direct Hydrolysis of Mesitylcopper (I) on $WO_3 \cdot 2H_2O$ Nanoleaves. *Chemosensors* **2023**, *11*, 495. https://doi.org/10.3390/chemosensors11090495

Academic Editor: Bilge Saruhan-Brings

Received: 13 July 2023
Revised: 23 August 2023
Accepted: 1 September 2023
Published: 9 September 2023

1. Introduction

Environmental pollution is one of the biggest challenges the world faces today. Despite efforts to reduce emissions, harmful substances are continually introduced into the air, water, and soil. This problem is getting worse with each passing year as a result of progressing industrialization and urbanization. These two processes are the main cause of emission of pollutants like: N_2O, NOx, SO_2, H_2S, NH_3, CO, CO_2, O_3, volatile organic compounds (VOCs), or particulate matter into the air [1]. These species enter the living organisms in various ways, negatively affecting their health. Moreover, some of these substances are greenhouse gases, which directly or indirectly affect the heat budget of our planet [2]. Therefore, there is an urgent need to develop new, more efficient, and economical technologies to limit the emission of pollutants into the air. In order to monitor the effectiveness of these efforts it is also important to measure the air pollution levels at proper spatial and temporal scales. As compared to laboratory-based analyses (e.g., techniques

based on gas chromatography), the use of miniaturized gas sensors provides several advantages. These devices can be implemented on portable devices, monitoring networks, and mobile platforms (e.g., drones) in order to provide in situ data continuously and over large areas [3–7]. Therefore, the development of new sensing devices is a pivotal goal for many research teams around the world. Nanotechnology delivers promising tools for that purpose, including the development of MOS (i.e., metal oxide semiconductor) sensors [8,9].

It has been shown that designing a sensitive layer at the nanoscale leads to an increase in the gas sensing performance, especially for grains with a diameter smaller than 20 nm [10]. Under these conditions, the electron-depleted layer (for n-type semiconductors) extends from the surface to the core of the grains. This results in an increase in the electrical resistance of the sensitive layer as compared to those containing larger grains, in which a significant part of the material does not participate in the oxygen adsorption process. For reducing gas detection, the nanoscale-designed sensitive layers offer more ionic oxygen species that can oxidize the analyte. In this process, a large portion of electrons returns to the sensitive layer leading to a drastic decrease in its resistance, which, in turn, translates into greater sensitivity of the sensor. The detection efficiency of sensors based on metal oxide nanoparticles can be additionally increased by decorating the sensitive layer with precious metals (e.g., Ag, Au, Pt, Pd, etc.), doping with carbon-based nanomaterials (carbon nanotubes, graphene, etc.), or creating heterojunctions [8,11].

The research on hetero-nano-junctions allowed significant advances in many fields, including supercapacitors [12], photocatalysis [13], and of course, gas sensing [14]. It initially involved the mechanical mixing of nanoparticles made of different metal oxides and employing the resulting mixture as gas-sensitive layers [15]. Another strategy was to create the so-called double sensing layer, where a layer of one type of metal oxide was deposited on top of another [16,17]. Nowadays, more advanced systems are usually considered, e.g., core–shell nanostructures or metal oxide nanoparticles decorated with smaller nanoparticles of the second phase [18]. Among many possible combinations, the $CuWO_4$ decorated WO_3 sensors have been intensively studied in recent years. For example, Duanmu [19] describes the gas-sensing properties of the $CuWO_4$@WO_3 nanocomposite prepared by a simple hydrothermal route. The sensor exhibited a three times higher response towards n-butanol as compared to the sensitive layer composed of pristine WO_3. Kumar [20] proposes $CuWO_4/WO_{3-x}$ films, prepared by reactive magnetron sputtering, for hydrogen sensing and proves its enhanced performance towards this gas as compared to pristine CuO and WO_3. Finally, Wang [21] studies the role of electron transfer behavior induced by CO chemisorption on visible-light-driven CO conversion over WO_3 and $CuWO_4/WO_3$ in order to explain its higher gas sensing performance.

The present manuscript describes a simple route for the preparation of Cu_2O@$WO_3 \cdot H_2O$ nanocomposite by modifying a synthesis protocol we have recently developed [22]. The method is based on direct hydrolysis of metal–organic precursor on $WO_3 \cdot 2H_2O$ nanoleaves. The hydrolysis took place at the expense of water molecules incorporated within the crystal lattice of the tungsten (VI) oxide dihydrate. Detailed characterization of the prepared material allows the extraction of information on its synthesis mechanism, morphology, and chemical composition. The described nanocomposite has been used as a gas-sensitive layer. During in situ heating, Cu_2O@$WO_3 \cdot H_2O$ transforms to $CuWO_4$@WO_3. Tests performed in the presence of one reducing and one oxidizing gas confirm the n-n type heterojunction formed between $CuWO_4$ and WO_3. The heterojunction influences significantly the gas-sensing properties of the nanocomposite as compared to the single-MOS-phase-containing sensors (i.e., WO_3 and CuO). Additionally, the experiments performed in the dark and under UV light irradiation suggest that the nanocomposite can serve as a dual sensor for the detection of CO and NO_2, respectively. The paper also describes the gas sensing mechanisms of the $CuWO_4$@WO_3 sensor deduced from gas response data analyses. Finally, possible directions for further improvement of future sensing layers for gas detection devices are proposed.

2. Experimental Section

Three nanomaterials have been prepared and used as gas-sensitive layers, namely $WO_3 \cdot 2H_2O$ nanoleaves (NLs), $Cu_2O@WO_3 \cdot 2H_2O$ nanocomposite (NCs), and Cu_2O nanoparticles (NPs). Their synthesis procedures have been described in Sections 2.1.1–2.1.3, respectively. As gas-sensitive layers, these nanomaterials are exposed to high operating temperatures. Therefore, we investigated the phase changes in the $WO_3 \cdot 2H_2O$ nanoleaves (NLs) and $Cu_2O@WO_3 \cdot 2H_2O$ nanocomposite (NCs) during their thermal treatment at temperatures up to 500 °C (see Section 2.2). The as-prepared and calcinated nanomaterials have been characterized in detail as described in Section 2.3. The preparation of gas sensors and description of gas test set-up have been provided in Sections 2.4 and 2.5, respectively.

2.1. Preparation of Nanomaterials

The $WO_3 \cdot 2H_2O$ nanoleaves (NLs) have been prepared through an ion exchange route as described by Chemseddine [23] and modified by Choi and co-workers [24]. The Cu_2O nanoparticles (NPs) have been produced by controlled hydrolysis of mesitylcopper (I) (CuMes) at room temperature under argon atmosphere and in the presence of an organic solvent (anisole). The $Cu_2O@WO_3 \cdot H_2O$ nanocomposite (NCs) has been synthesized by modifying a method described by Castello-Lux [22]. The latter is based on the in situ hydrolysis of an organometallic precursor (here mesitylcopper (I)) in a dry organic solvent directly on a suspension of $WO_3 \cdot 2H_2O$ NLs.

2.1.1. Preparation of the $WO_3 \cdot 2H_2O$ Nanoleaves

Sodium tungstate dihydrate ($Na_2WO_4 \cdot 2H_2O$) was purchased from Sigma Aldrich (Darmstadt, Germany) and used without further purification. Its aqueous solution (5 mL Milli-Q water, 0.4 mol/L), was introduced at the top of the glass column (comprising a glass frit at the bottom and filled with an acidified ion exchange resin (DOWEX-50WX2, Sigma Aldrich). The eluent was let flow out at a fixed flow of 1 drop/2s. The sodium tungstate in the column is pushed across the resin with several 10 mL portions of Milli-Q water up to the recovery of the natural pH of distilled water. The pH of the eluate was controlled with pH test strips. When the pH reached a value of around 2, the eluate (around 30 mL) was collected into a glass bottle, closed tightly, and stirred in the dark using an orbital shaker (Benchmark Scientific BT302-E) at 150 rpm, at room temperature, for 72 h. During that time the yellow transparent solution transformed into a yellow colloidal solution with characteristic opalescent reflections. The solution was then centrifuged (5000 rpm, 5 min, 25 °C) and the resulting precipitate was washed 3 times with 20 mL of Milli-Q water, and eventually with 20 mL of ethanol (Sigma Aldrich). Finally, the powder was dried under vacuum using a Schlenk line for 15 min. At the end, 444 mg of a yellow powder of $WO_3.2H_2O$ was obtained.

2.1.2. Preparation of the $Cu_2O@WO_3 \cdot H_2O$ Nanocomposite

In the glovebox, 100 mg of $WO_3 \cdot 2H_2O$ NLs were placed in a glass centrifugation tube and mixed with 5 mL of anhydrous toluene (collected from a solvent purification system, i.e., Braun MB-SPS-800, MBRAUN, Garching, Germany)). The tube was closed tightly and placed in ultrasonic bath for 20 min. In the meantime, in the glovebox, 40 mg (0.5 molar equivalent/W atom) of CuMes (Nanomeps, Toulouse, France) was weighed in a small beaker and mixed with 1 mL of anhydrous toluene. The as-prepared CuMes solution was added to the $WO_3 \cdot 2H_2O$ NLs solution and stirred in the dark using orbital shaker at 150 rpm, at room temperature, under argon atmosphere, for 3 h. During that time the solution changed color from yellow to khaki green. The solution was then centrifuged (3000 rpm, 5 min, 25 °C) and the precipitate was washed 3 times with 5 mL of the anhydrous toluene under argon atmosphere and 3 times with ethanol under ambient atmosphere. Finally, the product was dried under vacuum using Schlenk tube line for 15 min. An amount of 106 mg of pistachio green powder was obtained. The preparation procedure of the $Cu_2O@WO_3 \cdot H_2O$ nanocomposite is schematically represented in Figure 1.

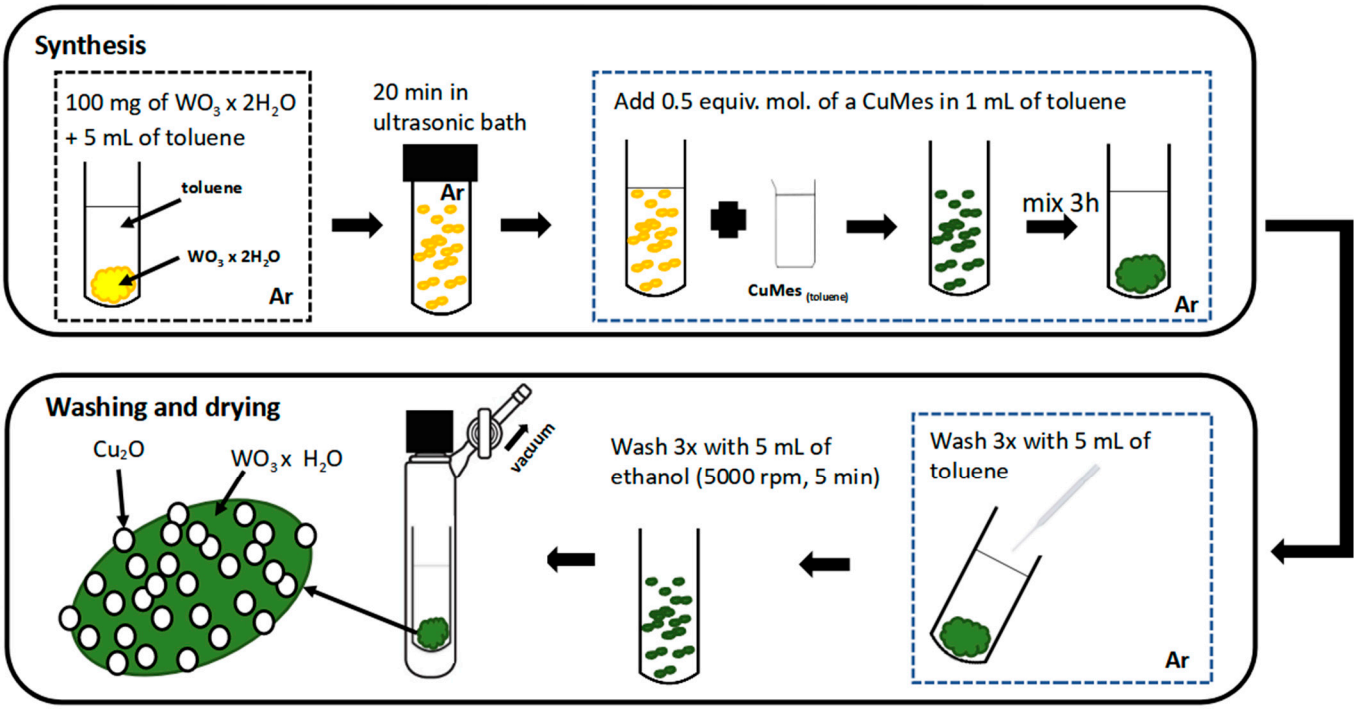

Figure 1. Preparation of the $Cu_2O@WO_3 \cdot H_2O$ nanocomposite by the exposure of the $WO_3 \cdot 2H_2O$ NLs to the CuMes precursor (**up**) and washing and drying procedure of the prepared nanomaterials (**down**).

2.1.3. Preparation of the Cu_2O nanoparticles

In the glovebox, in a small beaker, 100 mg of CuMes was mixed with 2 mL of anhydrous anisole (Sigma Aldrich). The beaker was placed in a homemade flat-bottomed reactor. Using a microsyringe, a drop (80 µL) of degassed Milli-Q water was distributed on the walls of the reactor under argon atmosphere. After 24 h, an orange colloidal solution was obtained. The solution was centrifuged (1000 rpm, 5 min, 25 °C) and the precipitate was washed twice with the anhydrous anisole under argon atmosphere and finally, dried using Schlenk tube line for 45 min. An amount of 25 mg of a brick red powder was obtained.

2.2. Calcination of the As-Prepared $Cu_2O@WO_3 \cdot H_2O$ Nanomaterials

The $Cu_2O@WO_3 \cdot H_2O$ nanocomposite was calcinated at 100 °C, 200 °C, 300 °C, 400 °C, and 500 °C. The experiments were performed under ambient atmosphere using a ramp of temperature of 2 °C/min. Samples were heated from room temperature to the target temperature and maintained at this temperature for 60 min. For comparison, the pristine $WO_3 \cdot 2H_2O$ nanoleaves were heat-treated following the same procedure. The characterization of the crystallographic phases was tracked by XRD analyses for both nanomaterials.

2.3. Characterization Methods

Transmission electron microscopy (TEM) images were taken using a JEOL 1400 microscope operating at 120 kV (JEOL, Ltd., Tokyo, Japan). The morphology, particle size, and size distribution were all determined using TEM images. The latter is calculated using more than 100 particles from each sample. A JEOL 2100F microscope operating at 200 kV was used to achieve high-resolution transmission electron microscopy (HRTEM). For Z-contrast, the system includes a probe corrector and a STEM HAADF detector (scanning TEM high-angle annular dark field). An EDX (energy dispersion X-ray) analysis system is also included in the system. Field emission gun scanning electron microscopy (FEG-SEM) images were captured using an SEM JEOL JSM 7800f (Tokyo, Japan) microscope operating at 10 kV.

The SXFive CAMECA® Electronic Microprobe (Genevilliers, France) was used for electron microprobe analyses. It uses a beam diameter of 600 nm and a voltage of 15 kV. It has five wavelength dispersive spectrometers with six different crystals, providing elemental studies ranging from B to U with detection limits of 0.01% by weight or atomic percentage. The results of this study are an average of 10 measurements per sample.

The powder diffraction patterns were acquired using the MPDPro PANalytical® with Cu-Kα radiation (Worcestershire, United Kingdom), fitted with a diffracted beam graphite monochromator. The data were gathered between 10 and 70 (0.016 θ/s) in the 2θ configuration.

The thermogravimetric analyses (TGA) were performed on a Setaram thermobalance (SETARAM Engineering, France) with a 5 °C/min ramp. The samples were heated from room temperature to 800 °C and held there for 30 min. Throughout the experiment, weight loss and heating rate were continuously measured.

2.4. Gas Sensors Preparation

Nanomaterials were drop deposited manually on miniaturized MEMS (micro-electro-mechanical) silicon substrates using metal oxide pastes prepared as follows:

- Amounts of 50 mg of the $WO_3 \cdot 2H_2O$ NLs were mixed with 35 µL of ESL 401 (Electro-Science Laboratories) binder (provided by the Laplace Laboratory (Toulouse, France)).
- Amounts of 50 mg of the $Cu_2O@WO_3 \cdot H_2O$ NCs were mixed with 55 µL of ESL 401 binder.
- Amounts of 25 mg of the Cu_2O NPs were mixed with 25 µL of the Milli-Q water and 15 µL of ESL 401 binder.

The ratio of oxide powder and binder amount was determined experimentally in order to prepare metal oxide pastes of adequate texture and viscosity.

The miniaturized silicon platform used in this investigation was created by the MICA group at the Laboratoire d'Analyse et d'Architecture des Systèmes, LAAS-CNRS. The die is 22 mm in diameter and incorporates a 1.4 m thick dielectric membrane ($SiNx/SiO_2$) designed for optimal thermal insulation of the heated area. Between the bottom dielectric membrane and the passivation top layer (silicon dioxide), a spiral-shaped platinum heater is buried. This heater structure can withstand temperatures of up to 700 °C while consuming as little as 55 mW at working temperatures of 500 °C. The interdigitated platinum electrodes for sensitive layer measurement are deposited as a last step on top of the SiO_2 passivation layer and have a rounded form. A 10 µm distance between each electrode pole ensures stable contact with high resistive sensing layers [25].

2.5. Gas Test Set-Up

Gas tests were carried out with a system consisting of several gas bottles connected to mass flow controllers (QualiFlow) controlled by an Agilent Data Acquisition/Switch Unit 34970A (Santa Clara, CA, USA). Sensors are installed in a measurement cell that includes humidity and temperature sensors. An HP6642A tension controller (Hewlett Packard, Palo Alto, CA, USA) drives the integrated heaters. A National Instruments 6035E electronic card (Austin, TX, USA) connects a computation unit to the measurement cell.

Freshly manufactured sensitive layers were first conditioned by successive in situ heating from room temperature to 500 °C in air. Following that, the sensitive layer resistance on the device was stabilized by annealing at 500 °C in synthetic air (relative humidity, RH 50%) at a total gas flow rate of 1 L/min. Finally, controlled quantities of CO (reducing gas) and NO_2 (oxidizing gas) were applied to the sensors. The experiments were carried out at 50% RH and operating temperatures of 540 °C, 445 °C, 390 °C, 250 °C, and 110 °C.

The sensitive layers were then subjected to UV light (365 nm) emitted by a Schottky diode while still running at high temperatures. The UV-illuminated sensors were also exposed to the above-mentioned gases at controlled amounts and at 50% RH. The resistance of the sensor was measured before and after its exposure to a reducing/oxidizing gas

mixture in the presence and absence of UV light, and the normalized responses (Rn (%)) to each gas were calculated as resistance variations (1), i.e.,

$$R_n = \frac{(R_{air} - R_{gas})}{R_{air}} \cdot 100, \quad (1)$$

where R_{air} corresponds to the sensor resistance in synthetic air and R_{gas} corresponds to the sensor resistance in reducing/oxidizing gas mixture.

The results presented here were obtained by employing at least three sensors manufactured according to the procedure described above (Section 2.4).

3. Results and Discussion

Over the past 20 years, we developed a simple, one-pot metal–organic procedure for the preparation of metal oxide nanoparticles. This method is based on the hydrolysis or oxidation of metal–organic precursors at room temperature and in a controlled atmosphere. This approach has been used for the preparation of zinc, copper, iron, and tin oxides [26–30]. Some of them have been used as gas-sensitive layers and exhibited remarkable gas-sensing properties [28–31]. Recently, a modification of this approach led to the formation of new nanocomposites where zinc oxide nanoparticles were grown on $WO_3{\cdot}2H_2O$ nanoleaves [22]. Thanks to the water molecules incorporated in the crystal lattice of the $WO_3{\cdot}2H_2O$, the hydrolysis of the zinc precursor (dicyclohexyl zinc (II)) was performed directly on the nanoleaves support without further addition of water and surfactants. The materials used for this study were prepared following an adaptation of this protocol. The $Cu_2O@WO_3{\cdot}H_2O$ NCs were prepared by direct hydrolysis of CuMes on the $WO_3{\cdot}2H_2O$ NLs. This nanocomposite was then characterized and used as a sensitive layer.

3.1. Morphology and Chemical Composition

3.1.1. $WO_3{\cdot}2H_2O$ NLs

A detailed description of the morphology and chemical composition of the $WO_3{\cdot}2H_2O$ powder resulting from the condensation of tungstic acid (see Section 2.1.1) has been published earlier [19]. Therefore, only a short summary of these findings will be presented here.

The NLs tend to grow along the (010) planes parallel to each other so that they form two-dimensional (2 D) plate-like crystallites as evidenced by SEM observations and XRD analyses. Indeed, the microscopic images indicated the presence of leaf-shaped particles (with the dimensions of 700 ± 200 nm long, 500 ± 200 nm large, and 30 ± 10 nm thick), and the diffraction patterns exhibited clear exaltations of the (020), (030) and (040) planes which are characteristic for the monoclinic P2/m structure of $WO_3{\cdot}2H_2O$ (JCPDS card nº018-1420). The presence of structural water molecules has been confirmed by the thermogravimetric analyses. The thermogram depicted the presence of two dehydration steps with a weight loss of c.a. 6.7% each. The first step began at 40 °C, whereas the second started at 120 °C. The structural water molecules can be divided into two types. The first one corresponds to the interlamellar molecules located on the (020) planes and is characterized by low bounding energy. The second one is related to the coordinated water molecules, which require higher thermal energy to be removed from the crystal. These findings were in accordance with the ^{1}H NMR and Raman spectroscopy data. Additionally, upon heating, some interesting phase changes were observed. At 100 °C, a monohydrate phase ($WO_3{\cdot}H_2O$) corresponding to the Pmnb orthorhombic structure emerged (JCPDS card nº43-0679), whereas at 200 °C the anhydrous (WO_3) phase characteristic for the P21/n monoclinic structure appeared (JCPDS card no. 43-1035). The structure stabilized at ca. 320 °C and no further mass losses or phase changes were observed. However, at this temperature, the crystallinity of the product is rather low, and further heating up to 500 °C was necessary to increase the crystallite mean size.

3.1.2. $Cu_2O@WO_3 \cdot H_2O$ Nanocomposites (NCs)

According to the results described before we have concentrated our study on the reaction of CuMes (Cu(I)) with $WO_3 \cdot 2H_2O$ NLs only [22]. The yellow suspension of the NLs rapidly turns green after the addition of the CuMes solution (0.5 molar equivalent CuMes/W atom) (Figure 2). This color change is associated with the formation of W^{n+} ($n < 6$, mainly W^{5+}) species and suggests that the Cu^+ ions of the precursor are strongly oxophilic and capable of removing oxygen atoms from the WO_3 lattice and thus, forming the first Cu_2O germs [32,33].

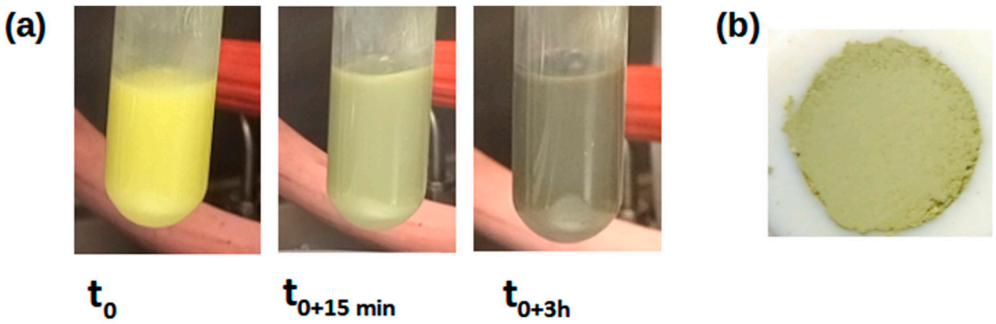

Figure 2. The color evolution of the $WO_3 \cdot 2H_2O$ NLs exposed to CuMes (0.5 molar equivalent CuMes/W atom) solution, where t_0—before CuMes solution was added to the $WO_3 \cdot 2H_2O$ NLs, $t_{0+15\ min}$—after 15 min of the reaction between the $WO_3 \cdot 2H_2O$ NLs and CuMes, t_{0+3h}—after 3 h of the reaction between the $WO_3 \cdot 2H_2O$ NLs and CuMes (**a**) and the image of the resulting powder after washing and drying steps (**b**).

The growth of the Cu_2O NPs on the NLs is clearly evidenced in the SEM images where additional nanostructures appear on the surface of the WO_3 supports (Figure 3a,b). Similar features are present in the TEM images (Figure 3c,d). The shape of the NLs is maintained after the decoration and there are no free Cu_2O NPs present aside from on the microscopy grid. Moreover, a 20 min. ultrasound treatment of the nanocomposite colloidal suspension does not affect its morphology, i.e., there are still no free Cu_2O NPs on the grid. These findings give evidence of the exclusive growth of the Cu_2O NPs over the WO_3 supports thanks to the very localized hydrolysis of the copper precursor.

The HRTEM images confirm the presence of the Cu_2O NPs on the WO_3 NLs (Figure 4a). The size of the Cu_2O NPs estimated from these images varies from 4 nm to even 16 nm (mean 7.8 $\pm$ 4.3 nm). Although they are rather homogeneously distributed on the support, some aggregates can be observed as well. Such an agglomeration has not been noticed for the $ZnO@WO_3 \cdot H_2O$ nanocomposite [22].

The HRTEM images also reveal the crystalline nature of the Cu_2O NPs growing at the edges of the WO_3 support (Figure 4b) and the FT study of such nanoparticles confirms the presence of crystalline planes corresponding to the cubic structure of Cu_2O (Figure 4c). Finally, the EDX analyses of these nanoparticles reveal the exclusive presence of copper and oxygen (Figure 4d—zone 1). When the Cu_2O is located above the support, the EDX analysis reveals the simultaneous presence of copper, tungsten, and oxygen giving yet more evidence for the growth of the Cu_2O NPs on the WO_3 NLs (Figure 4d—zone 2).

The XRD analyses of the $WO_3 \cdot 2H_2O$ NLs, $WO_3 \cdot H_2O$ NLs, and $Cu_2O@WO_3 \cdot H_2O$ NCs suggest that during the reaction of the $WO_3 \cdot 2H_2O$ NLs with CuMes solution, a spontaneous phase transformation from monoclinic to orthorhombic takes place. Indeed, the peak at $2\theta = 13.2^\circ$ characteristic for the $WO_3 \cdot 2H_2O$ NLs phase is not present on the diffractograms of both the $WO_3 \cdot H_2O$ NLs and $Cu_2O@WO_3 \cdot H_2O$ NCs (Figure 5). The increase in the CuMes content in the reaction medium (up to 1.0 molar equivalent CuMes/W atom) does not cause further phase transformations. These results agree with Castello-Lux [22] and suggest that only one type of structural water molecule (interlamellar water groups) is consumed. However, the XRD diagram does not reveal peaks corresponding to the Cu_2O NPs suggesting their crystalline domains are probably too small for this technique.

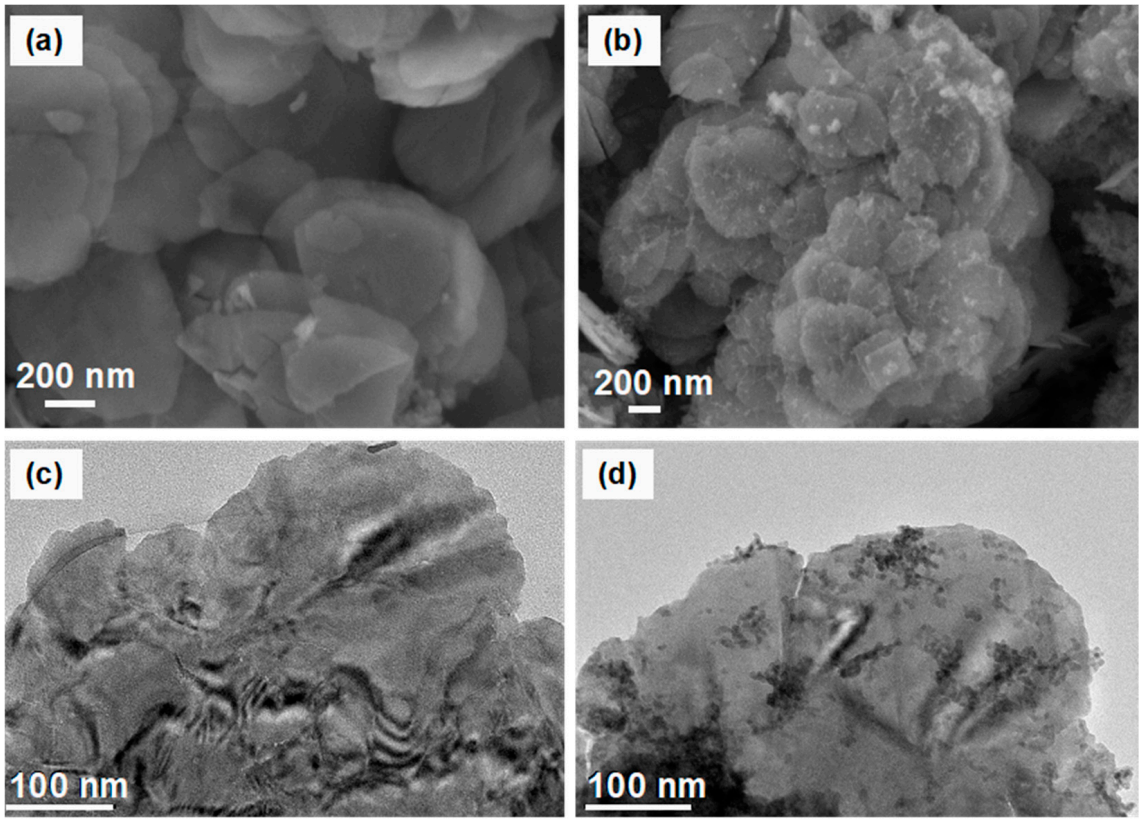

Figure 3. SEM (**a**,**b**) and TEM (**c**,**d**) images of $WO_3 \cdot 2H_2O$ NLs support (**a**,**c**) and $Cu_2O@WO_3 \cdot H_2O$ nanocomposite (0.5 molar equivalent CuMes/W atom) (**b**,**d**).

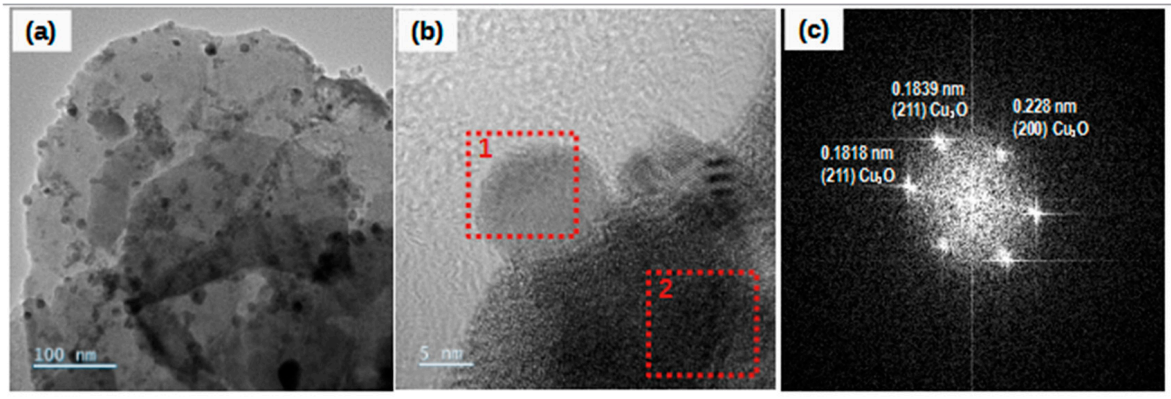

(d)

Zone 1 element	% weight	σ	Zone 2 element	% weight	σ
Cu	82.6	0.2	Cu	54.9	0.1
W	-	-	W	31.9	0.1
O	17.4	0.2	O	13.2	0.1

Figure 4. (**a**,**b**) HRTEM images of the $Cu_2O@WO_3 \cdot H_2O$ nanocomposite (0.5 molar equivalent CuMes/W atom), (**c**) FT image of the particle located in the zone 1 (indicated by the red square in (**b**) showing cubic crystal planes), (**c**) EDX analyses of the zone 1 and zone 2 (indicated by the red squares in (**d**).

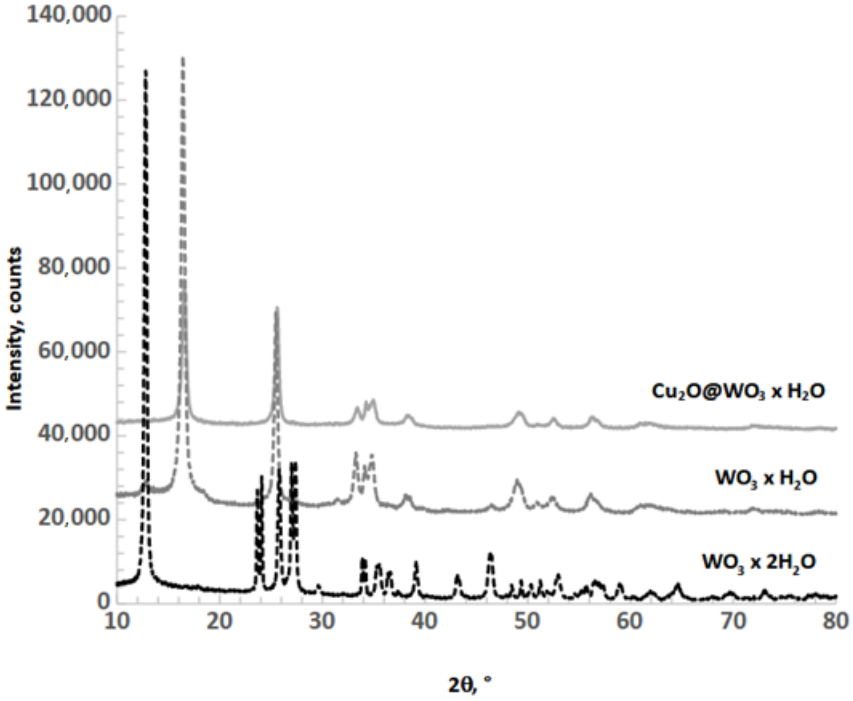

Figure 5. XRD diagrams of $WO_3 \cdot 2H_2O$ NLs, $WO_3 \cdot H_2O$ NLs, and $Cu_2O@WO_3 \cdot H_2O$ nanocomposite (0.5 molar equivalent CuMes/W atom).

The TGA analyses confirmed that only the interlamellar water molecules (whose removal begins at 40 °C) from $WO_3 \cdot 2H_2O$ NLs are involved in the reaction. The coordinated water molecules remain unaffected during the nanocomposite synthesis regardless of the amount of copper precursor used (i.e., 0.25; 0.5; 1.0 molar equivalent CuMes/W). Therefore, the thermogram of the reaction product exhibits only one dehydration step that starts at 120 °C (Figure 6).

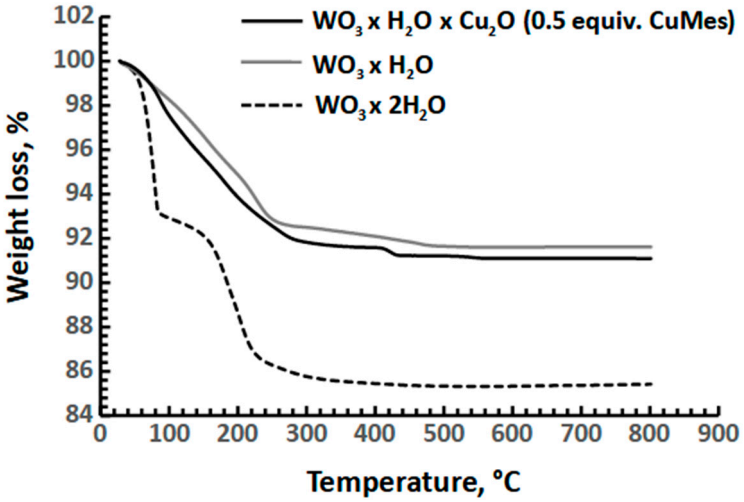

Figure 6. TGA analysis of $WO_3 \cdot 2H_2O$ NLs, $WO_3 \cdot H_2O$ NLs, and $Cu_2O@WO_3 \cdot H_2O$ nanocomposite (0.5 molar equivalent CuMes/W).

The theoretical weight loss for one water molecule corresponds to c.a. 6.7% of the total mass of $WO_3 \cdot 2H_2O$. A very close value is experimentally measured by the TGA analyses of the $WO_3 \cdot 2H_2O$ NLs (Table 1), i.e., 7.3% and 7.0% for the interlamellar water molecules (labile water) and coordinated water molecules, respectively. When 0.25, 0.5, and 1.0 molar equivalent CuMes/W atom is reacted with the $WO_3 \cdot 2H_2O$ the weight loss of the labile

water molecules drops to 1.8%, 1.2%, and 1.1%, respectively (Table 1). This means that about 80% of the labile water molecules are consumed by the copper precursor. At the same time, the content of the coordination water remains close to the theoretical value of 6.7%. The decrease in the labile water content was associated with the increase in the Cu_2O loading on the support as revealed by the elementary analyses (Table 1). The content of copper doubled (from 5.6% to 13.1% weight) with the increase in CuMes in the reaction medium from 0.25 to 0.5 molar equivalent CuMes/W. Further, an increase in CuMes from 0.5 to 1.0 molar equivalent CuMes/W led to a further increase in the copper content in the nanocomposite, but the value did not double as in the previous case and reached only 17.0%.

Table 1. TGA and elementary analyses of the $Cu_2O@WO_3 \cdot H_2O$ nanocomposite after reaction of $WO_3 \cdot 2H_2O$ with increasing amounts of CuMes (molar equivalent).

	TGA			Microanalysis		
CuMes Amount (Molar Equivalent)	**H_2O/Cu Molar Ratio**	**Low T° H_2O Weight Loss (%)**	**High T° H_2O Weight Loss (%)**	**Cu (% wt.)**	**W (% wt.)**	**O (% wt.)**
0	-	7.3	7.0	-	77.3	19.2
0.25	3.2	1.8	6.6	5.6	68.0	23.9
0.5	1.7	1.2	6.8	13.1	65.3	20.0
1.0	0.8	1.1	7.3	17.0	54.7	21.2

The limiting condition in the reaction of CuMes with the $WO_3 \cdot 2H_2O$ NLs is the number of labile water molecules for the copper precursor hydrolysis. With 0.25 and 0.5 molar equivalent CuMes/W, the molar ratio of water to copper precursor reaches 3.2 and 1.7, respectively. The labile water content is in excess and thus, the entire copper precursor is hydrolyzed. The increase in the CuMes to 1.0 molar equivalent CuMes/W leads to the decrease in the molar ratio of water to copper precursor to 0.8. Therefore, the quantity of water is not enough to decompose the entire copper precursor in the reaction medium.

3.1.3. Cu_2O NPs

In order to assess the gas sensing properties of $Cu_2O@WO_3 \cdot H_2O$ NCs with $WO_3 \cdot 2H_2O$ NLs and pure Cu_2O NPs, we have also synthesized the latter by the hydrolysis of an organic solvent solution of CuMes by adding controlled amounts of water in the synthesis reactor (see Section 2.1.3). In these conditions, a brick red powder is obtained after a few hours of reaction. When stored in air, the red suspension turns black within a few hours, suggesting the fast oxidation of the Cu_2O powder into CuO oxide [34]. The final product is composed of agglomerated nanoparticles with a mean diameter of 8.4 ± 2.6 nm (calculated from the TEM images) (Figure 7).

3.2. Transformation of the $Cu_2O@WO_3 \cdot H_2O$ NCs into $CuWO_4@WO_3$ NCs

Thermal treatment of the $Cu_2O@WO_3 \cdot H_2O$ NCs was performed at up to 500 °C in the air in order to investigate the evolution of the nanocomposite material that may occur on the gas sensing device during the initial in situ heating of the sensitive layer (see Section 2.5). For comparison, the $WO_3 \cdot 2H_2O$ powder followed the same heating procedure. The XRD analyses of the nanocomposite prepared with 0.5 molar equivalent CuMes/W atom and after its thermal treatment at different temperatures are presented in Figure 8a. The phase transformations were observed during the thermal treatment. Between 200 and 300 °C a transformation from orthorhombic to monoclinic phase with low crystallinity is noticed. This signature is characteristic of the WO_3 NLs [22]. The XRD diagrams do not reveal peaks corresponding to Cu_2O or CuO NPs or any other phase at temperatures up to 400 °C. However, at 500 °C a new phase appeared next to the WO_3 one. Indeed, the comparison of XRD diagrams of the $Cu_2O@WO_3 \cdot H_2O$ and $WO_3 \cdot 2H_2O$ powders after their thermal

treatment at 500 °C reveals the simultaneous presence of the WO_3 monoclinic phase that remains oriented along the (002) planes, in addition to the $CuWO_4$ triclinic phase (JCPDS No 88-0269) with a series of characteristic peaks at 2 theta values of 19.0° (100), 24.0° (110), 25.9° (101), 28.7° (111), 30.1° (111), 31.6° (111), 32.1° (111), 35.6° (012), 36.8° (002), 39.8° (120) and 42.9° (102) (Figure 8b). The strong intensity and narrow width of $CuWO_4$ diffraction peaks indicate that the resulting products are of high crystallinity. Indeed, the crystallite mean size of the $CuWO_4$ achieved at 500 °C is 37.8 ± 6.9 nm, which is higher than the crystallite mean size of the WO_3 support (19.6 ± 3.5). It may be concluded that during the thermal treatment, the Cu_2O nanoparticles react with the WO_3 support to yield a new mixed oxide $CuWO_4$ phase. According to Kolt'sova and Nipan [35], in the CuO-WO_3 systems two mixed oxide phases can be formed at elevated temperatures up to 900 °C, i.e., yellow–green $CuWO_4$ and black Cu_3WO_6. In the presence of an excess of the initial WO_3 phase (the case of this study), the $CuWO_4$ phase is preferentially formed, as confirmed by the XRD studies of the nanocomposite after its thermal treatment at 500 °C as well as by the green color of the final powder.

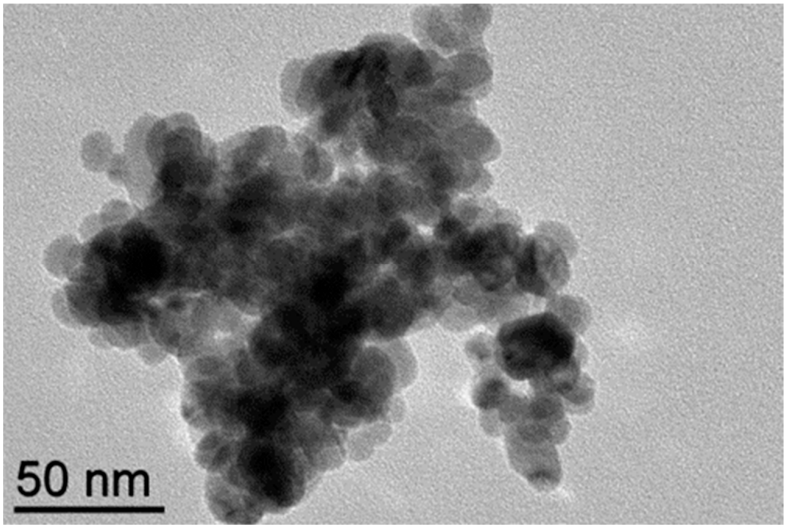

Figure 7. TEM image of the Cu_2O nanoparticles.

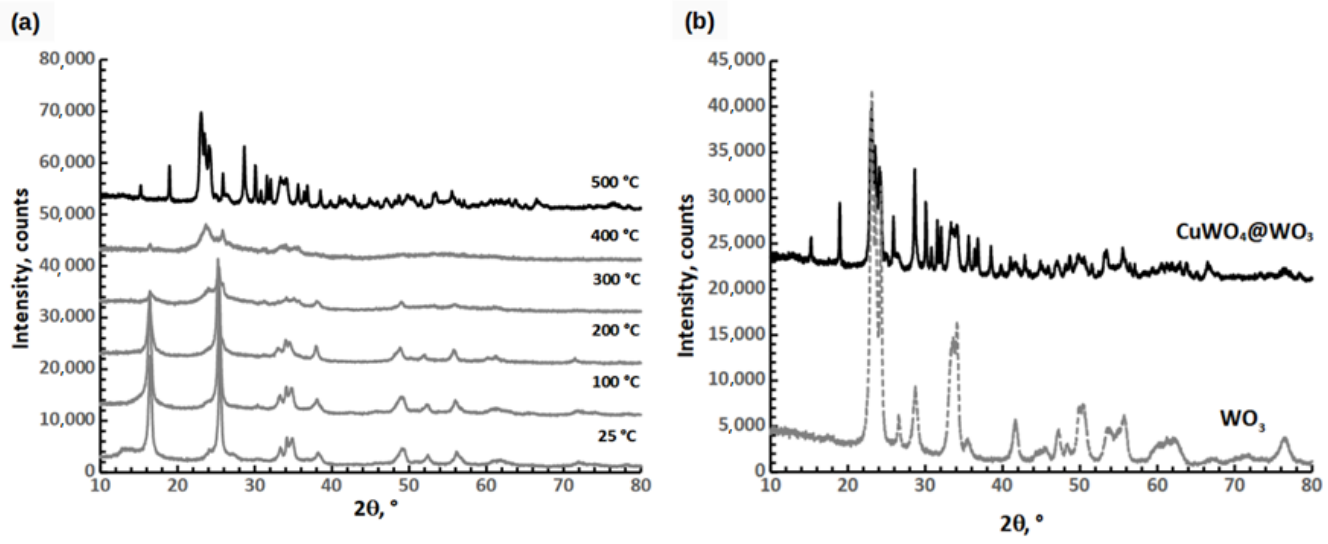

Figure 8. (**a**) XRD analyses of $Cu_2O@WO_3 \cdot H_2O$ NCs before and after thermal treatment at 100, 200, 300, 400, and 500 °C, (**b**) XRD analyses of WO_3 NLs and $CuWO_4@WO_3$ NCs obtained after the thermal treatment of $WO_3 \cdot 2H_2O$ and $Cu_2O@WO_3 \cdot H_2O$ at 500 °C, respectively.

During the thermal treatment, the morphology of the nanocomposite has evolved as evidenced by SEM images (Figure 9). It seems that some of the nanoleaves have started to melt during the thermal treatment and have lost their initial form (for reference, see Figure 3 a,b). However, additional structures are evidenced on the WO_3 supporting layers as well. The STEM image of the nanocomposite after thermal treatment suggests that two phases can be distinguished within the material (Figure 10a). The STEM-EDX images reveal that the lighter regions are reached in copper (Figure 10b) whereas the darker ones are composed mainly of tungsten (Figure 10c). Therefore, the STEM-EDX analyses confirm the data obtained with the XRD analyses.

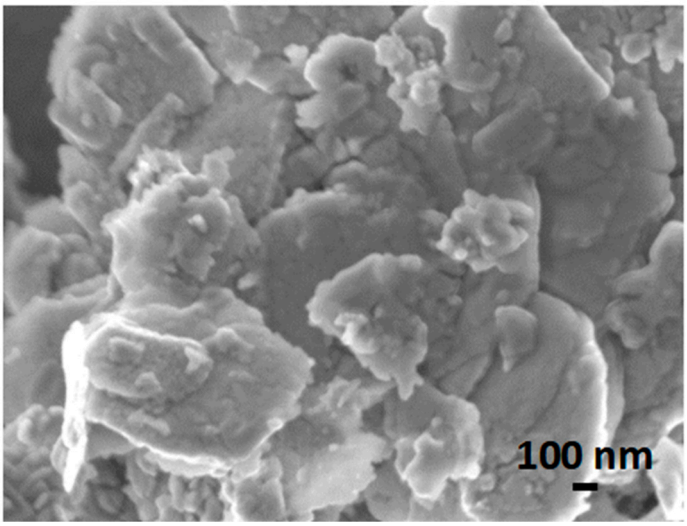

Figure 9. SEM image of the $CuWO_4@WO_3$ nanocomposite prepared by thermal treatment of $Cu_2O@WO_3{\cdot}H_2O$ at 500 °C.

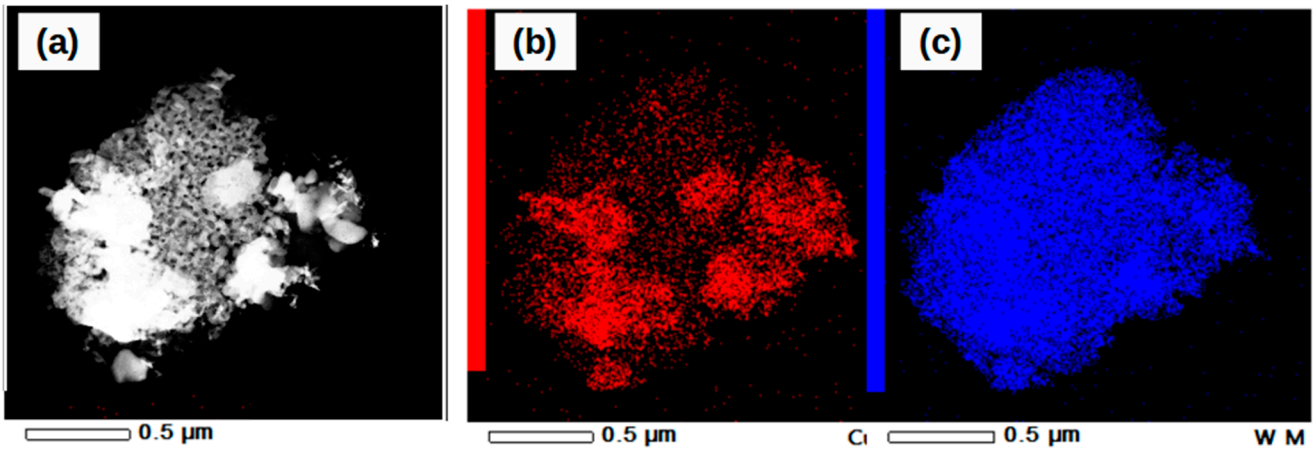

Figure 10. STEM image (**a**) and STEM-EDX cartography of copper (**b**) and tungsten (**c**) of the $CuWO_4@WO_3$ nanocomposite prepared by thermal treatment of $Cu_2O@WO_3{\cdot}H_2O$ at 500 °C.

3.3. Evaluation of the Gas Sensing Properties of NLs, NCs, and NPs

The Cu_2O NPs, $WO_3{\cdot}2H_2O$ NLs, and $Cu_2O@WO_3{\cdot}H_2O$ NCs have been deposited on silicon gas sensing devices (see Section 2.4). After deposition, the layers have been in situ annealed by operating the integrated Pt heater up to 550 °C. This step allows the complete removal of organic residues from the deposited powders. During this thermal process, phase transitions occur for each sensitive material: Cu_2O are oxidized to CuO, $WO_3{\cdot}2H_2O$ are dehydrated to WO_3 and $Cu_2O@WO_3{\cdot}H_2O$ nanocomposite is transformed into $CuWO_4@WO_3$ nanocomposite. Afterward, the sensors were exposed to one oxidative

(0.4 ppm NO_2) and one reductive gas (10 ppm CO) in synthetic air at different operating temperatures and relative humidity (RH) of 50%.

In air, at the operating temperature of 390 °C and 50% RH, the CuO sensor presents a resistance of only c.a. 1 kOhm (Table 2). The resistance of the CuO sensor increases in the reductive atmosphere and decreases in the oxidative one which is characteristic of the p-type semiconductor gas sensors [36]. Under the same conditions, the resistance of the WO_3 sensors exhibits a resistance of c.a. 800–1200 kOhms (Table 2). The resistance of the WO_3 sensor increases in the presence of NO_2 and decreases in the presence of CO which is characteristic for the n-type semiconductor gas sensors. At 390 °C, the resistance of the $CuWO_4$@WO_3 nanocomposite sensors reaches a few tens of MOhms (Table 2) which can be associated with the formation of the n-n heterojunction established between the WO_3 support (band gap 2.6–3.0 eV) [37] and $CuWO_4$ (band gap 2.2 eV) loading (see Section 3.5) [38]. The resistance of the $CuWO_4$@WO_3 nanocomposite sensor increases in the presence of the oxidative gas and decreases when exposed to the reductive gas. Therefore, the sensor behaves like an n-type semiconductor gas sensor.

Table 2. Resistance (kOhms) of the CuO, WO_3, and $CuWO_4$@WO_3 sensors in air at different operating temperatures and RH = 50%.

Sensor	Temperature				
	t = 540 °C	**t = 445 °C**	**t = 390 °C**	**t = 250 °C**	**t = 110 °C**
CuO	<1	<1	<1	3	16
WO_3	580	612	828	2064	1120
$CuWO_4$@WO_3	ca. 10,000	ca. 18,000	r	r	r

r—extremely high sensor resistance (tens of MOhms) and problems with baseline stabilization.

For the CuO sensor, the highest sensitivity towards 10 ppm CO was achieved at the relatively low operating temperature of 250 °C (Rn = 34%). However, for these conditions, the sensor was also sensitive to 0.4 ppm NO_2 (Rn = 12%). Moreover, at lower operating temperatures (i.e., 250 °C and 110 °C) the sensor's response and recovery are very sluggish. At higher operating temperatures, the CuO sensor becomes more selective towards CO, but the resistance variations in the presence of this reductive gas are much smaller as well. Indeed, the normalized response towards CO at 390 °C is equal to 18% and decreases with further increase in the operating temperature (Figure 11a,b, Table 3). However, at higher operating temperatures (i.e., 390 °C and above) the sensor's response and recovery improve significantly. Having all this in mind, it was concluded that the CuO nanoparticles may serve as an efficient CO-sensitive layer when operated at 390 °C. This is in accordance with previous studies [29,39,40].

Table 3. Normalized responses (Rn(%)) of CuO, WO_3, and $CuWO_4$@WO_3 n-n heterojunction sensors towards 10 ppm CO and 0.4 ppm NO_2 at different operating temperatures and RH = 50%.

Analyzed Gas	**CO**			**NO_2**		
Sensor	***CuO***	***WO_3***	***$CuWO_4$@WO_3***	***CuO***	***WO_3***	***$CuWO_4$@WO_3***
t = 540 °C	9%	-	18%	-	16%	180%
t = 445 °C	14%	-	30%	-	80%	620%
t = 390 °C	18%	5%	r	3%	225%	r
t = 250 °C	34%	7%	r	12%	500% *	r
t = 110 °C	c.a. 13% *	c.a. 13% *	r	c.a. 17%*	c.a.1900% *	r

- No response, * due to the sluggish response and/or recovery the sensor signal under target gas is not stabilized and thus underestimated, r—extremely high sensor resistance and problems with baseline stabilization.

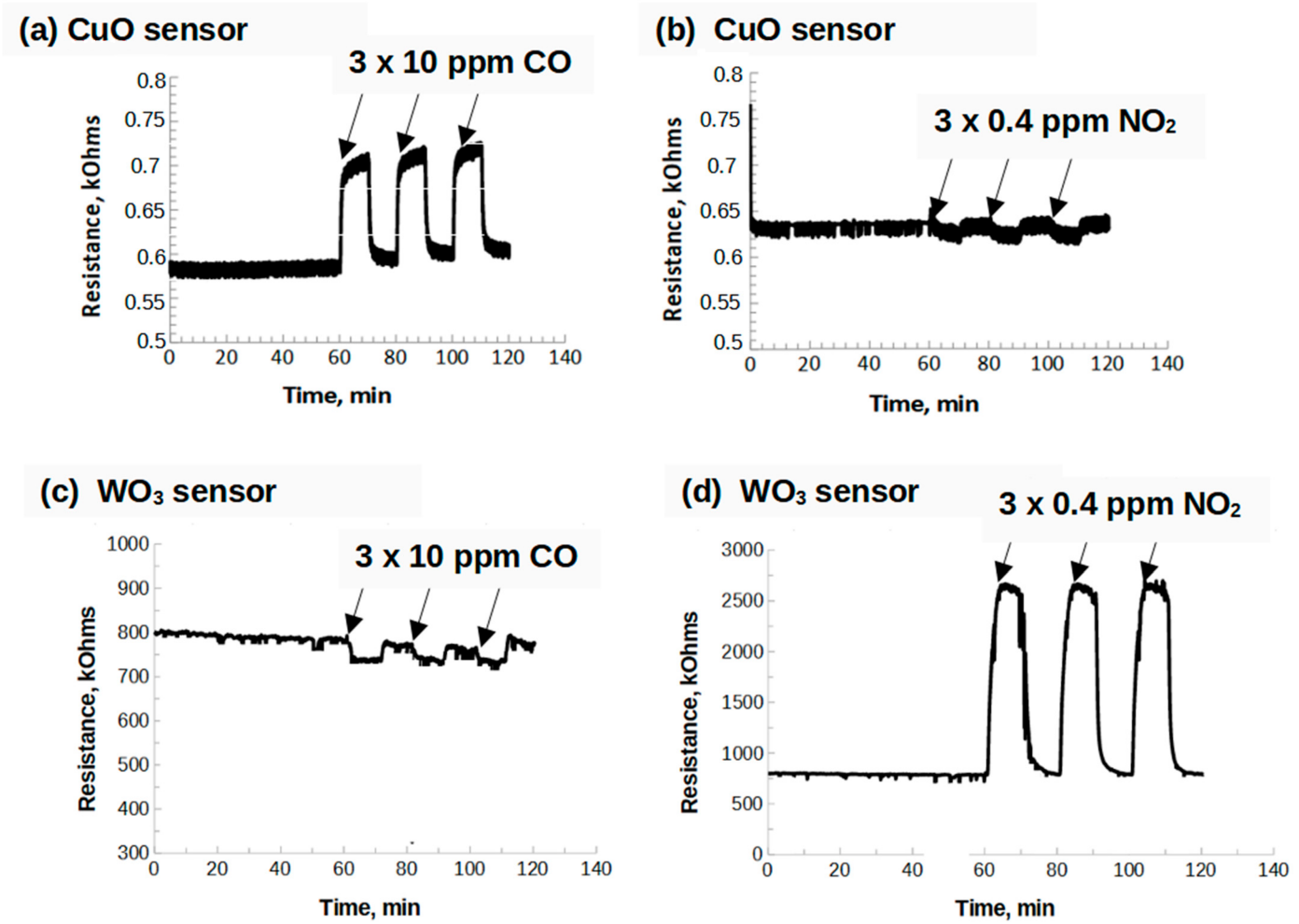

Figure 11. Gas sensing performance of CuO (**a**,**b**) and WO_3 (**c**,**d**) sensors towards 10 ppm CO (**a**,**c**) and 0.4 ppm NO_2 (**b**,**d**) gases at operating temperature of 390 °C and RH = 50%.

The WO_3 sensor exhibits a remarkably high response towards 0.4 ppm NO_2 and very weak or no response to 10 ppm of CO (Table 3). Indeed, at lower temperatures (110 and 250 °C), the resistance of the sensor in an oxidative atmosphere increases from hundreds of kOhms to several MOhms suggesting that this sensor can be a potential candidate for selective detection of NO_2 at ppb levels. However, the recovery of the sensor at lower temperatures is quite sluggish. The normalized response of the WO_3 sensor towards NO_2 decreases with the increase in the operating temperature but still reaches very high values even at elevated temperatures (i.e., 225% at 390 °C) whereas the response and recovery time are more vigorous than at lower temperatures (Figure 11c,d, Table 3). Having all this in mind, it was concluded that the WO_3 sensor is an efficient NO_2-sensitive layer when operating at 390 °C. Indeed, tungsten oxide material has been identified as one of the most sensitive materials for NO_2 detection [41–43].

The resistance of the $CuWO_4$@WO_3 nanocomposite sensors in air at 110, 250, and 390 °C is very high (several tens of MOhms), and for these conditions, the sensor response to tested gases is very weak (data not shown). Therefore, it is better to operate the device at more elevated temperatures (i.e., 445 and 540 °C, RH 50%). Indeed, at higher temperatures, the resistance of the sensor drops to a dozen MOhms (Table 2). The $CuWO_4$@WO_3 nanocomposite sensor is sensitive to both tested gases with higher resistance variations at 445 °C than at 540 °C (Figure 12a, Table 3). Importantly, at 445 °C, the sensitivity of the $CuWO_4$@WO_3 nanocomposite towards CO and NO_2 is higher than the one for CuO and WO_3 sensors at their optimal operating temperature (i.e., 390 °C). The high sensitivity can

be driven by the presence of the n-n junction established between the WO_3 support and the $CuWO_4$ crystals (see Section 3.5). The $CuWO_4$@WO_3 n-n heterojunction sensor also exhibits significantly higher sensitivity towards NO_2 (Rn=620%, 445 °C) as compared to CO (Rn = 30%, 445 °C), but is less selective than the other tested sensitive layers; with CuO responding only to CO (at 390 °C and above) and WO_3 being almost completely selective to NO_2 (at all tested temperatures). The $CuWO_4$@WO_3 nanocomposite sensor exhibits, therefore, gas sensing properties of both CuO and WO_3 sensitive layers. To the best of our knowledge, such a comparison of gas sensing properties of the $CuWO_4$@WO_3 sensor towards oxidative and reductive gases has never been performed before. Studies have rather focused on a unique type of gas, e.g., n-butanol [19], CO [21] or H_2 [19].

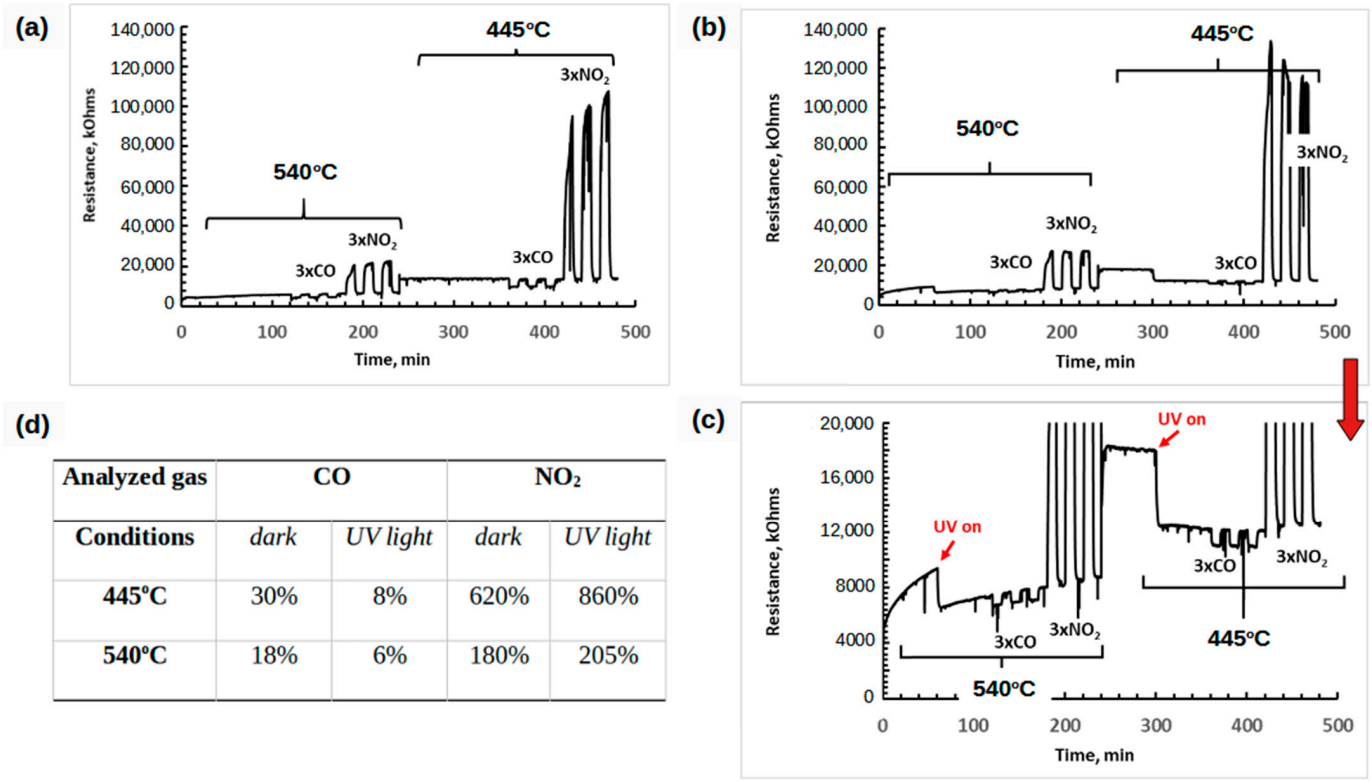

(d)

Analyzed gas	CO		NO_2	
Conditions	*dark*	*UV light*	*dark*	*UV light*
445°C	30%	8%	620%	860%
540°C	18%	6%	180%	205%

Figure 12. (**a**) Gas sensing performance of $CuWO_4$@WO_3 NCs towards 10 ppm CO and 0.4 ppm NO_2 at 445 °C and 500 °C (RH = 50%) in the dark and (**b**,**c**) under UV light irradiation (**c**) is a zoom of low resistances values of b curve) and (**d**) normalized response (Rn (%)) calculated from (**a**–**c**).

3.4. Gas Sensing Responses of $CuWO_4$@WO_3 NCs under UV Light Irradiation

Figure 12 shows gas sensing performances of $CuWO_4$@WO_3 nanocomposite sensor to CO and NO_2 at 445 °C and RH = 50% in the dark and under UV light irradiation conditions.

The resistance of the sensor decreases rapidly under UV light exposition. The UV irradiation of $CuWO_4$@WO_3 nanocomposite produces photo-generated electrons, resulting in an increase in the surface electron density of the material. With the introduction of 10 ppm CO, the resistance of the sensor decreases slightly and the normalized response towards this gas reaches only c.a. 8%. Therefore, the gas sensing performance of the $CuWO_4$@WO_3 nanocomposite sensitive layer towards this reductive gas worsens in the presence of UV light. Under the same conditions, the response towards 0.4 ppm NO_2 remains high and reaches c.a. 860% which is slightly better than before the sensor irradiation (i.e., 620%). UV irradiation increases the selectivity and sensitivity of the sensor toward the oxidizing gas. Moreover, the $CuWO_4$@WO_3 nanocomposite-sensitive layer can be used as a double sensor. In the dark, it can detect CO (provided NO_2 is not present in the air), whereas under UV irradiation it can selectively detect NO_2 in the presence of CO. The enhanced sensitivity

towards NO_2 for $CuWO_4/WO_3$ NCs and under UV light irradiation was described earlier (e.g., [38]).

3.5. The Proposed Gas Sensing Mechanism of $CuWO_4$@WO_3 NCs Sensor

The mechanism of the n-type MOS sensor operation can be briefly described as follows. Under normal conditions, atmospheric oxygen is adsorbed on the surface of the sensitive layer, where it is reduced to one of its ionized forms:

$$O_{2\,(gas)} \rightarrow O_{2\,(ads)} \quad (2)$$

$$O_{2\,(gas)} + e^- \rightarrow {O_2}^-{}_{(ads)} \quad (3)$$

$${O_2}^-{}_{(gas)} + e^- \rightarrow 2{O}^-{}_{(ads)} \quad (4)$$

$$O^-\,(gas) + e^- \rightarrow {O^{2-}}_{(ads)} \quad (5)$$

As a result of this process, the sensitive layer is deprived of its charge carriers, i.e., electrons, which increases the resistance of the sensor. When the sensitive layer is designed on a microscale, oxygen is adsorbed only on the surface of the metal oxide grains and, consequently, electrons are removed only from a certain depth, called the Debye length. This region may decrease or increase when, in addition to oxygen, the adsorption of other gases is undergone. As a consequence, the resistance of the sensor can then increase or decrease in the presence of oxidizing or reducing species, respectively.

It has been shown that designing a sensitive layer at the nanoscale significantly changes the sensor performance [10]. In the case of nanoparticles, the electron-depleted layer includes both the surface and the inside of the grains. Therefore, the sensor possesses increased resistance as compared to sensitive layers built of larger grains (in which a significant part does not participate in the oxygen adsorption process material). Additionally, for the $CuWO_4$@WO_3 nanocomposite, the formation of the n-n heterojunctions further modifies the performances of the sensor. When the $CuWO_4$ particles are formed at the surface of the WO_3 support, the electron transfer from the WO_3 support to the mixed oxide ($CuWO_4$) appears [19–21]. An electron accumulation layer and an electron depletion layer are formed at the interface between $CuWO_4$ and WO_3, respectively. As shown in Figure 13a the formation and the extension of the depletion layer within the WO_3 would narrow the electron pathway and increase the resistance of the $CuWO_4$@WO_3 nanocomposite sensor. The loading of the Cu_2O nanoparticles on the support is rather important (13.1%) and thus, promotes the formation of the mixed oxide species on the WO_3 surface upon heating. This leads to the formation of an important number of n-n junctions where electrons from the WO_3 support are transferred to the $CuWO_4$ structures and trapped on the adsorbed oxygen species. Therefore, it is necessary to heat the $CuWO_4$@WO_3 nanocomposite sensors to higher temperatures than the CuO and WO_3 which is the main drawback of the developed material. This problem can be addressed in the future by optimizing the number of n-n heterojunctions. Indeed, the $CuWO_4$ loading on the WO_3 support and, therefore, the resistance of the NCs sensor, can be easily tuned by changing the amount of the CuMes used for the synthesis (see Section 3.1.2). These changes may, however, modify some other parameters of the $CuWO_4$@WO_3 nanocomposite sensors including their sensitivity, selectivity, and/or capability to work as a dual sensor.

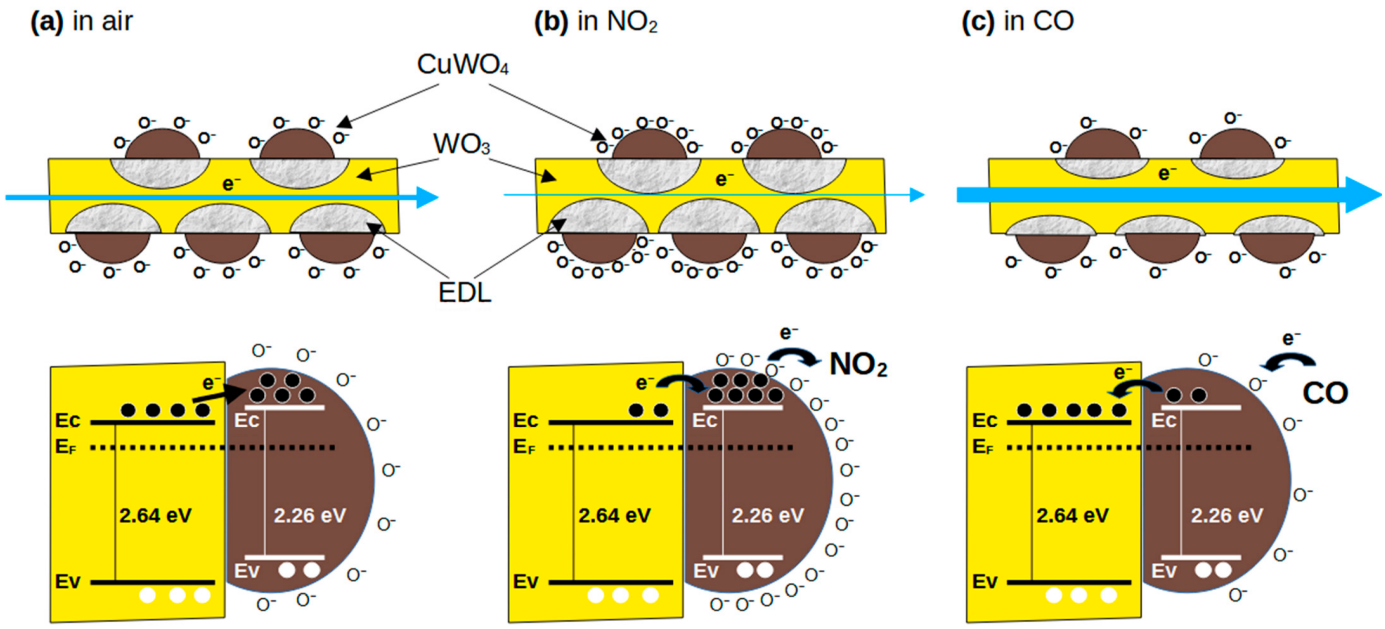

Figure 13. Illustration of gas sensing mechanism and energy level structure of $CuWO_4$@ WO_3 nanostructured heterojunction: (**a**) the extension of electron depletion layer (EDL) in air, (**b**) the increase in the EDL thickness in oxidizing gas, (**c**) the decrease in the EDL in reducing gas. The blue arrow on the top images indicates the current flow level across the sample: the larger the arrow, the higher the current flow.

Upon exposure to NO_2, the gas adsorbs at the surface of the sensor, principally at the $CuWO_4$, where it is reduced using both the oxygen species and electrons from the sensitive layer, leading to the formation of the NO_2^- species [44,45]:

$$NO_{2(ads)} + e^- \rightarrow NO_2^-{}_{(ads)} \quad (6)$$

$$NO_{2(ads)} + O_2^-{}_{(ads)} + 2e^- \rightarrow NO_2^-{}_{(ads)} + 2O^-{}_{(ads)} \quad (7)$$

$$NO_{2(ads)} + O^-{}_{(ads)} + 2e^- \rightarrow NO_2^-{}_{(ads)} + O^{2-}{}_{(ads)} \quad (8)$$

This forces further transfer of electrons from WO_3 to $CuWO_4$, leading to an even extended depletion layer of the charge carriers in the WO_3 support. This effect generates a higher resistance of the NC structure compared to pure WO_3 (Figure 13b).

Upon exposure to CO, the chemisorbed oxygen species react with CO, which oxidizes to CO_2. The CO_2 molecules are removed from the surface and release electrons back to the $CuWO_4$@WO_3 NCs:

$$2CO_{(gas)} + O_2^-{}_{(ads)} \rightarrow 2CO_{2(gas)} + e^- \quad (9)$$

$$CO_{(gas)} + O^-{}_{(ads)} \rightarrow CO_{2(gas)} + e^- \quad (10)$$

$$CO_{(gas)} + O^{2-}{}_{(ads)} \rightarrow CO_{2(gas)} + 2e^- \quad (11)$$

The net result is a narrowing of the depletion layer and an even larger resistance change as compared to the pristine WO_3 material (Figure 13c).

3.6. The Proposed Gas Sensing Mechanism of UV Irradiated $CuWO_4$@WO_3 NCs Sensor

The 365 nm UV diode was chosen since it is the most often employed UV wavelength to create electron/hole pairs within the ZnO or WO_3 metal oxide gas sensors applied to NO_2

gas sensing [46–48]. Indeed, the WO_3 NLs of this study present a rather high optical band gap energy (Eg) close to 3.0 V, which was experimentally measured by the Kulbelka–Munk function from the diffuse reflection spectroscopy of the sample [49]. The enhancement of NO_2 detection in the presence of UV illumination is associated with the formation of photo-generated electrons at the composite surface that promote the adsorption of O_2^- species [50]. However, the baseline resistance of the $CuWO_4$@WO_3 nanocomposite sensor decreases under UV illumination. This indicates that created O_2^- species are either rapidly desorbed and/or that photogenerated electrons are injected in the conduction band of the composite [51]. Compared to CO, the NO_2 gas molecule must react more efficiently with photo-generated O_2^- species to form NO_2^- species which are responsible for a larger resistance increase in the sensitive layer (as compared to the measurements performed in the dark). It was also demonstrated that the presence of heterojunctions in the composite materials increases the lifetime of the electron/hole carriers and therefore, leads to a higher generation rate of adsorbed O_2^- ionic species at the semiconductor surface able to react with NO_2 [52]. The CO detection of the sensor is degraded in that case due to the overall lowering of the baseline resistance and the presence of an important number of electrons in the conduction band of the composite as compared to the measurements performed in the dark.

On the other hand, it has also been noted that during UV illumination another redox reaction occurs on the surface of the sensitive layer that leads to the formation of the NO_3^- species [53–55]:

$$NO_{2(ads)} + {O_2}^-{}_{(hv)} + e^- \rightarrow {NO_3}^-{}_{(ads)} + O^- \quad (12)$$

This reaction may occur as well in the dark but to a lesser extent. This changes after sensor UV illumination, i.e., although the NO_2^- species are still produced, the NO_3^- species formation significantly increases [56,57]. Therefore, NO_2 can interact with the sensitive layer in different ways. Increased NO_2 response may thus also be explained by the fact that previously described reactions (Equations (6)–(8) and (12)) simultaneously took place when the sensors were UV illuminated.

4. Conclusions and Future Work

The paper describes the preparation, characterization, and application of three different gas sensing materials (i.e., CuO NPs, WO_3 NLs, and $CuWO_4$@WO_3 NCs) towards one oxidizing (0.4 ppm NO_2) and one reducing (10 ppm CO) gas. Special attention is given to the preparation of the Cu_2O@$WO_3 \cdot H_2O$ nanocomposite and to the resulting $CuWO_4$@WO_3 n-n heterojunction sensitive layer obtained after thermal treatment. The latter exhibits interesting gas-sensing properties, especially upon exposure to UV light illumination. Several conclusions can be drawn from this work:

(1) The adaptation of an earlier described procedure [19] allowed for the preparation of the new Cu_2O@$WO_3 \cdot H_2O$ nanocomposite. This proposed protocol can be used as a versatile method for the preparation of metal oxide nanocomposites by in situ hydrolysis of metal–organic precursors on the $WO_3 \cdot 2H_2O$ nanoleaves.

(2) The thermal treatment of the prepared nanocomposite onto the gas sensing device led to the formation of the $CuWO_4$ mixed oxide grafted on the WO_3 support ($CuWO_4$@WO_3).

(3) The $CuWO_4$@WO_3 nanocomposite exhibits intermediate gas sensing properties compared to the CuO and WO_3 sensors. However, at higher temperatures (i.e., 445 °C), the nanocomposite sensor is more sensitive to CO and NO_2 than other tested sensors. This was explained by the formation of the n-n heterojunction between the $CuWO_4$ and WO_3.

(4) Upon UV light irradiation of the $CuWO_4$@WO_3 nanocomposite the resistance of the sensor in air decreases but its sensitivity towards CO gas is worsened. At the same time, the sensitivity and selectivity towards NO_2 increased which was associated with the photo-generation of electrons within the nanocomposite. Therefore, the $CuWO_4$@WO_3 sensitive layer can be used as a dual gas sensor.

(5) At lower operating temperatures, the CuO and WO_3 (at an operating temperature of 390 °C) layers can also serve as efficient gas-sensitive layers for the selective detection of CO and NO_2, respectively.

All the sensors of this study, including the $CuWO_4$@WO_3 nanocomposite one, are versatile sensitive layers that can be integrated into a gas sensors array dedicated to electronic nose platforms. Further research should focus on the optimization of $CuWO_4$ loading on the WO_3 support.

Author Contributions: Funding acquisition, writing—original draft preparation, investigation, J.J.; conceptualization and methodology, P.F. and K.C.-L.; Visualization, J.J. and V.C., writing—review and editing, J.J., K.C.-L., K.F., M.L.K., V.C., P.M., I.S. and P.F. All authors have read and agreed to the published version of the manuscript.

Funding: This project has received funding from the European Union's Horizon 2020 research and innovation program under the Marie Skłodowska-Curie grant agreement No. 101033564. This work was also partly supported by the LAAS-CNRS micro- and nano-technologies platform member of the French RENATECH network.

Institutional Review Board Statement: Not applicable.

Informed Consent Statement: Not applicable.

Data Availability Statement: Data are contained within the article.

Conflicts of Interest: The authors declare no conflict of interest.

References

1. Manisalidis, I.; Stavropoulou, E.; Stavropoulos, A.; Bezirtzoglou, E. Environmental and Health Impacts of Air Pollution: A Review. *Front. Public Health* **2020**, *8*, 14. [CrossRef]
2. McMichael, A.J.; Lindgren, E. Climate change: Present and future risks to health, and necessary responses. *J. Intern. Med.* **2011**, *270*, 401–413. [CrossRef] [PubMed]
3. Szczurek, A.; Gonstał, D.; Maciejewska, M. The Gas Sensing Drone with the Lowered and Lifted Measurement Platform. *Sensors* **2023**, *23*, 1253. [CrossRef] [PubMed]
4. Kaliszewski, M.; Włodarski, M.; Młyńczak, J.; Jankiewicz, B.; Auer, L.; Bartosewicz, B.; Liszewska, M.; Budner, B.; Szala, M.; Schneider, B.; et al. The Multi-Gas Sensor for Remote UAV and UGV Missions—Development and Tests. *Sensors* **2021**, *21*, 7608. [CrossRef] [PubMed]
5. Szulczyński, B.; Gębicki, J. Currently Commercially Available Chemical Sensors Employed for Detection of Volatile Organic Compounds in Outdoor and Indoor Air. *Environments* **2017**, *4*, 21. [CrossRef]
6. Szulczyński, B.; Wasilewski, T.; Wojnowski, W.; Majchrzak, T.; Dymerski, T.; Namieśnik, J.; Gębicki, J. Different Ways to Apply a Measurement Instrument of E-Nose Type to Evaluate Ambient Air Quality with Respect to Odour Nuisance in a Vicinity of Municipal Processing Plants. *Sensors* **2017**, *17*, 2671. [CrossRef] [PubMed]
7. Seesaard, T.; Goel, N.; Kumar, M.; Wongchoosuk, C. Advances in gas sensors and electronic nose technologies for agricultural cycle applications. *Comput. Electron. Agric.* **2022**, *193*, 106673. [CrossRef]
8. Miller, D.R.; Akbar, S.A.; Morris, P.A. Nanoscale metal oxide-based heterojunctions for gas sensing: A review. *Sens. Actuators B Chem.* **2014**, *204*, 250–272. [CrossRef]
9. Zappa, D.; Galstyan, V.; Kaur, N.; Munasinghe Arachchige, H.M.M.; Sisman, O.; Comini, E. "Metal oxide-based heterostructures for gas sensors"—A review. *Anal. Chim. Acta* **2018**, *1039*, 1–23. [CrossRef]
10. Sharma, S.; Madou, M. A new approach to gas sensing with nanotechnology. *Philos. Trans. R. Soc. A Math. Phys. Eng. Sci.* **2012**, *370*, 2448–2473. [CrossRef]
11. Zhao, Z.; Yang, H.; Wei, Z.; Xue, Y.; Sun, Y.; Zhang, W.; Li, P.; Gong, W.; Zhuiykov, S.; Hu, J. NH3 Sensor Based on 3D Hierarchical Flower-Shaped n-ZnO/p-NiO Heterostructures Yields Outstanding Sensing Capabilities at ppb Level. *Sensors* **2020**, *20*, 4754. [CrossRef]
12. Ojha, G.P.; Pant, B.; Acharya, J.; Lohani, P.C.; Park, M. Solvothermal-localized selenylation transformation of cobalt nickel MOFs templated heterointerfaces enriched monoclinic Co_3Se_4/$CoNi_2Se_4$@activated knitted carbon cloth for flexible and bi-axial stretchable supercapacitors. *Chem. Eng. J.* **2023**, *464*, 142621. [CrossRef]
13. Dasineh Khiavi, N.; Katal, R.; Kholghi Eshkalak, S.; Masudy-Panah, S.; Ramakrishna, S.; Hu, J. Visible Light Driven Heterojunction Photocatalyst of CuO–Cu_2O Thin Films for Photocatalytic Degradation of Organic Pollutants. *Nanomaterials* **2019**, *9*, 1011. [CrossRef]
14. Yang, S.; Lei, G.; Xu, H.; Lan, Z.; Wang, Z.; Gu, H. Metal Oxide Based Heterojunctions for Gas Sensors: A Review. *Nanomaterials* **2021**, *17*, 1026. [CrossRef]

15. De Lacy Costello, B.P.J.; Ewen, R.; Jones, P.R.; Ratcliffe, N.; Wat, R.K. A study of the catalytic and vapour-sensing properties of zinc oxide and tin dioxide in relation to 1-butanol and dimethyldisulphide. *Sens. Actuators B Chem.* **1999**, *61*, 199–207. [CrossRef]
16. Maziarz, W. TiO_2/SnO_2 and TiO_2/CuO thin film nano-heterostructures as gas sensors. *Appl. Surf. Sci.* **2019**, *480*, 361–370. [CrossRef]
17. Kwon, H.; Yoon, J.-S.; Dong, Y.L.; Kim, Y.; Beak, C.-K.; Kim, J.Y. An array of metal oxides nanoscale hetero p-n junctions toward designable and highly-selective gas sensors. *Sens. Actuators B Chem.* **2018**, *255*, 1663–1670. [CrossRef]
18. Meng, F.-J.; Xin, R.-F.; Li, S.-X. Metal Oxide Heterostructures for Improving Gas Sensing Properties: A Review. *Materials* **2023**, *16*, 263. [CrossRef] [PubMed]
19. Duanmu, F.; Shen, Z.; Liu, Q.; Zhong, S.; Ji, H. A WO_3-$CuWO_4$ nanostructured heterojunction for enhanced n-butanol sensing performance. *Chin. Chem. Lett.* **2020**, *31*, 1114–1118. [CrossRef]
20. Kumar, N.; Haviar, S.; Zeman, P. Three-Layer PdO/$CuWO_4$/CuO System for Hydrogen Gas Sensing with Reduced Humidity Interference. *Nanomaterials* **2021**, *11*, 3456. [CrossRef]
21. Wang, Z.; Wang, X.; Wang, H.; Chen, X.; Dai, W.; Fu, X. The role of electron transfer behavior induced by CO chemisorption on visible-light-driven CO conversion over WO_3 and $CuWO_4/WO_3$. *Appl. Catal. B Environ.* **2020**, *265*, 118588. [CrossRef]
22. Castello Lux, K.; Fajerwerg, K.; Hot, J.; Ringot, E.; Bertron, A.; Collière, V.; Kahn, M.L.; Loridant, S.; Coppel, Y.; Fau, P. Nano-Structuration of WO_3 Nanoleaves by Localized Hydrolysis of an Organometallic Zn Precursor: Application to Photocatalytic NO_2 Abatement. *Nanomaterials* **2022**, *12*, 4360. [CrossRef] [PubMed]
23. Chemseddine, A.; Morineau, R.; Livage, J. Electrochromism of colloidal tungsten oxide. *Solid State Ion.* **1983**, *9*, 357–361. [CrossRef]
24. Choi, Y.-G.; Sakai, G.; Shimanoe, K.; Miura, N.; Yamazoe, N. Preparation of aqueous sols of tungsten oxide dihydrate from sodium tungstate by an ion-exchange method. *Sens. Actuators B Chem.* **2002**, *87*, 63–72. [CrossRef]
25. Menini, P.; Chalabi, H.; Yoboué, P.; Scheid, E.; Conédéra, V.; Salvagnac, L.; Aguir, K. High Performances of New Microhotplate for Gas Sensors. In Proceedings of the 22nd European Conference on Solid state Transducers (EUROSENSORS XXII), Dresden, Germany, 7–10 September 2008.
26. Kahn, M.L.; Monge, M.; Colliere, V.; Senocq, F.; Maisonnat, A.; Chaudret, B. Size- and Shape-Control of Crystalline Zinc Oxide Nanoparticles: A New Organometallic Synthetic Method. *Adv. Funct. Mater.* **2005**, *15*, 458–468. [CrossRef]
27. Casterou, C.; Collière, V.; Lecante, L.; Coppel, Y.; Eliat, P.A.; Gauffre, F.; Kahn, M.L. Improved Transversal Relaxivity for Highly Crystalline Nanoparticles of Pure γ-Fe_2O_3 Phase. *Chemistry* **2015**, *14*, 18855–18861. [CrossRef] [PubMed]
28. Ryzhikov, A.; Jońca, J.; Kahn, M.L.; Fajerwerg, K.; Chaudret, B.; Chapelle, A.; Menini, P.; Shim, C.H.; Gaudon, A.; Fau, P. Organometallic synthesis of ZnO nanoparticles for gas sensing: Towards selectivity through nanoparticles morphology. *J. Nanopart. Res.* **2015**, *17*, 280. [CrossRef]
29. Jońca, J.; Ryzhikov, A.; Palussiere, S.; Esvan, J.; Fajerwerg, K.; Menini, P.; Kahn, M.L.; Fau, P. Organometallic Synthesis of CuO Nanoparticles: Application in Low-Temperature CO Detection. *ChemPhysChem* **2017**, *18*, 2658–2665. [CrossRef]
30. Jońca, J.; Ryzhikov, A.; Kahn, M.L.; Fajerwerg, K.; Chapelle, A.; Menini, P.; Fau, P. SnO_2 "Russian Doll" Octahedra Prepared by Metalorganic Synthesis: A New Structure for Sub-ppm CO Detection. *Eur. J. Chem.* **2016**, *22*, 10127–10135. [CrossRef]
31. Sendi, A.; Fau, P.; Fajerwerg, P.; Kahn, M.L.; Menini, P. Detection and Discrimination of Formaldehyde with CuO/SnO_2 dual layers MOS Gas Sensors Operated with a Pulsed Temperature Modulation. In Proceedings of the Conference: 6th International Conference on Sensors Engineering and Electronics Instrumentation Advances (SEIA' 2020), Porto, Portugal, 23–25 September 2020.
32. Escalante, G.; Lopez, R.; Demesa, F.N.; Villa-Sanchez, G.; Castrejon-Sanchez, V.H.; Vivaldo de la Cruz, I. Correlation between Raman spectra and color of tungsten trioxide (WO3) thermally evaporated from a tungsten filament. *AIP Adv.* **2021**, *11*, 055103. [CrossRef]
33. Castillero, P.; Rico-Gavira, V.; Lopez-Santos, C.; Barranco, A.; Perez-Dieste, V.; Escudero, C.; Espinos, J.P.; Gonzalez-Elipe, A.R. Formation of subsurface W5+ species in gasochromic Pt/WO_3 thin films exposed to hydrogen. *J. Phys. Chem. C* **2017**, *121*, 15719–15727. [CrossRef]
34. Ojha, G.P.; Muthurasu, A.; Tiwari, A.P.; Pant, B.; Chhetri, K.; Mukhiya, T.; Dahal, B.; Lee, M.; Park, M.; Kim, H.-K. Vapor solid phase grown hierarchical CuxO NWs integrated MOFs-derived CoS2 electrode for high-performance asymmetric supercapacitors and the oxygen evolution reaction. *Chem. Eng. J.* **2020**, *399*, 125532. [CrossRef]
35. Kol'tsova T., N.; Nipan, G.D. System CuO-WO_3. *Inorg. Mater.* **1999**, *35*, 471–472.
36. Umar, A.; Algadi, H.; Kumar, R.; Akhtar, M.S.; Ibrahim, A.A.; Albargi, H.; Alhamami, M.A.M.; Alsuwian, T.; Zeng, W. Ultrathin Leaf-Shaped CuO Nanosheets Based Sensor Device for Enhanced Hydrogen Sulfide Gas Sensing Application. *Chemosensors* **2021**, *9*, 221. [CrossRef]
37. Yadav, A.A.; Hunge, Y.M.; Kang, S.W. Porous Nanoplate-like Tungsten Trioxide/Reduced Graphene Oxide Catalyst for Sonocatalytic Degradation and Photocatalytic Hydrogen Production. *Surf. Interfaces* **2021**, *24*, 101075. [CrossRef]
38. Liu, Y.; Li, X.; Li, X.; Shao, C.; Han, C.; Xin, J.; Lu, D.; Niu, L.; Tang, Y.; Liu, Y. Highly permeable $WO_3/CuWO_4$ heterostructure with 3D hierarchical porous structure for high-sensitive room-temperature visible-light driven gas sensor. *Sens. Actuators B Chem.* **2022**, *365*, 131926. [CrossRef]
39. Oosthuizen, D.N.; Motaung, D.E.; Swart, H.C. Selective detection of CO at room temperature with CuO nanoplatelets sensor for indoor air quality monitoring manifested by crystallinity. *Appl. Surf. Sci.* **2019**, *466*, 545–553. [CrossRef]

40. Hou, L.; Zhang, C.; Li, L.; Du, C.; Li, X.; Kang, X.F.; Chen, W. CO gas sensors based on p-type CuO nanotubes and CuO nanocubes: Morphology and surface structure effects on the sensing performance. *Talanta* **2018**, *188*, 41–49. [CrossRef]
41. Abegg, S.; Klein Cerrejon, D.; Güntner, A.T.; Pratsinis, S.E. Thickness Optimization of Highly Porous Flame-Aerosol Deposited WO_3 Films for NO_2 Sensing at ppb. *Nanomaterials* **2020**, *10*, 1170. [CrossRef] [PubMed]
42. Zhao, S.; Shen, Y.; Zhou, P.; Zhong, X.; Han, C.; Zhao, Q.; Wei, D. Design of Au@WO_3 core−shell structured nanospheres for ppb-level NO_2 sensing. *Sens. Actuators B Chem.* **2019**, *282*, 917–926. [CrossRef]
43. Gonzalez, O.; Welearegay, T.G.; Vilanova, X.; Llobet, E. Using the Transient Response of WO_3 Nanoneedles under Pulsed UV Light in the Detection of NH_3 and NO_2. *Sensors* **2018**, *18*, 1346. [CrossRef]
44. Drewniak, S.; Drewniak, Ł.; Pustelny, T. Mechanisms of NO_2 Detection in Hybrid Structures Containing Reduced Graphene Oxide: A Review. *Sensors* **2022**, *22*, 5316. [CrossRef] [PubMed]
45. Zhang, F.; Lin, Q.; Han, F.; Wang, Z.; Tian, B.; Zhao, L.; Dong, T.; Jiang, Z. A flexible and wearable NO_2 gas detection and early warning device based on a spraying process and an interdigital electrode at room temperature. *Microsyst. Nanoeng.* **2022**, *8*, 40. [CrossRef]
46. Fan, C.; Shi, J.; Zhang, Y.; Quan, X.; Yang, J.; Zeng, M.; Zhou, Z.; Su, Y.; Wei, H.; Yang, Z. Fast and recoverable NO_2 detection achieved by assembling ZnO on $Ti_3C_2T_x$ MXene nanosheets under UV illumination at room temperature. *Nanoscale* **2022**, *14*, 3441–3451. [CrossRef] [PubMed]
47. Cai, Z.; Kim, K.-K.; Park, S. Room temperature detection of NO_2 gas under UV irradiation based on Au nanoparticle-decorated porous ZnO nanowires. *J. Mater. Res. Technol.* **2020**, *9*, 16289–16302. [CrossRef]
48. Su, P.-G.; Yu, J.-H. Enhanced NO_2 gas-sensing properties of Au-Ag bimetal decorated MWCNTs/WO_3 composite sensor under UV-LED irradiation. *Sens. Actuators A Phys.* **2020**, *303*, 111718. [CrossRef]
49. Castelló-Lux, K. Synthesis and Gold Decoration of Alternative Oxides to TiO_2 for the Photocatalytic Degradation of NO and NO_2 in Indoor Environment Conditions: Evaluation of the Efficiency and the Contribution of the Decoration on the Photocatalytic Activity. Ph.D. Thesis, Universite Paul Sabatier, Toulouse, France, 2022. Available online: https://www.theses.fr/2022ISAT0025 (accessed on 11 August 2023).
50. Xuan, J.; Zhao, G.; Sun, M.; Jia, F.; Zhou, T.; Yin, G.; Liu, B. Low-temperature operating ZnO-based NO_2 sensors: A review. *RSC Adv.* **2020**, *10*, 39786–39807. [CrossRef]
51. Bonaccorsi, L.; Malara, A.; Donato, A.; Donato, N.; Leonardi, S.G.; Neri, G. Effects of UV Irradiation on the Sensing Properties of In_2O_3 for CO Detection at Low Temperature. *Micromachines* **2019**, *10*, 338. [CrossRef] [PubMed]
52. Lu, G.; Xu, J.; Sun, J.; Yu, Y.; Zhang, Y.; Liu, F. UV-enhanced room temperature NO_2 sensor using ZnO nanorods modified with SnO_2 nanoparticles. *Sens. Actuators B Chem.* **2012**, *162*, 82–88. [CrossRef]
53. Sayago, I.; Santos, J.P.; Sánchez-Vicente, C. The Effect of Rare Earths on the Response of Photo UV-Activate ZnO Gas Sensors. *Sensors* **2022**, *22*, 8150. [CrossRef]
54. Cai, Z.; Park, J.; Park, S. Synthesis of Flower-like ZnO and Its Enhanced Sensitivity towards NO_2 Gas Detection at Room Temperature. *Chemosensors* **2023**, *11*, 322. [CrossRef]
55. Platonov, V.; Malinin, N.; Vasiliev, R.; Rumyantseva, M. Room Temperature UV-Activated NO_2 and NO Detection by ZnO/rGO Composites. *Chemosensors* **2023**, *11*, 227. [CrossRef]
56. Barsan, N.; Koziej, D.; Weimar, U. Metal oxide-based gas sensor research: How to? *Sens. Actuators B Chem.* **2007**, *121*, 18–35. [CrossRef]
57. Chizhov, A.; Kutukov, P.; Gulin, A.; Astafiev, A.; Rumyantseva, M. UV-Activated NO_2 Gas Sensing by Nanocrystalline ZnO: Mechanistic Insights from Mass Spectrometry Investigations. *Chemosensors* **2022**, *10*, 147. [CrossRef]